INTERNATIONAL JOURNAL FOR NUMERICAL METHODS IN FLUIDS
Int. J. Numer. Meth. Fluids 2003; **41**:615–632 (DOI: 10.1002/fld.458)

LES of the flow past a rectangular cylinder using the immersed boundary concept

D. G. E. Grigoriadis[1,2,*,†], J. G. Bartzis[1] and A. Goulas[2]

[1]*NCSR DEMOKRITOS, Ag.Paraskevi Attikis 15310, Athens, Greece*
[2]*Aristotle University of Thessaloniki, Greece*

SUMMARY

Incompressible turbulent flow past a long square cylinder is investigated using large eddy simulations (LES). Results are presented and compared with available experimental databases for a Reynolds number $Re_d = 22\,000$. The problem served as one of the validation cases for the development of a numerical code designed for efficient, parallel, three-dimensional N-S computations in complex geometrical configurations. In contrast with previous studies, the geometrical definition of the problem is established by the immersed boundary concept (IMB) while pressure solution is performed by a fast, fully parallel direct pressure solver. Calculations were performed with the widely applied Smagorinsky turbulence model and the filtered structure function model (FSF) which has not been previously applied to the flow case under consideration. In order to assess the potential of LES at its lowest (RANS), and highest (DNS) limit, different numerical resolutions were examined. Depending on the available resolution, either no-slip conditions or a modified Werner and Wengle approximate wall boundary condition was used. The predicted mean velocity and fluctuation profiles, force statistics and Strouhal numbers were found to be in very good agreement with the experimental data sets. Analysis of the results indicates that for time varying bluff-bodies flows that involve complex flow phenomena, successful large eddy simulations are not just possible, but can also achieve an excellent quality of results at a relatively low cost. Copyright © 2003 John Wiley & Sons, Ltd.

KEY WORDS: LES; rectangular cylinder; immersed boundary method; direct pressure solver; `FISHPAK`; parallel computing

1. INTRODUCTION

The flow around cylinders is a flow regime that frequently appears in various internal and external flows like heat exchangers, electronic devices, flow metres, buildings and other structural elements. It also forms one of the basic problems in aerodynamics because of the alternating forces that act on the body. Various experimental and numerical studies have been conducted in the literature on the flow around cylinders [1, 2]. This is mainly due to the orthogonal

* Correspondence to: D. G. E. Grigoriadis, National Centre of Scientific Research, Demokritos, Ag. Paraskevi Attikis, 15310 Athens, Greece.
† E-mail: dimokratis@hotmail.com

Received 26 May 2002
Revised 9 November 2002

geometrical configuration that can be treated with relatively simple grids. However, that geometric simplicity by no means implies a simple flow topology at the Re number considered. Several complex physical mechanisms appear in a periodical manner, like the formation of forced shear layers at the upwind corners, separation, recirculation, vortex shedding and eventual wake formation and growth behind the body. These flow patterns are building blocks for most of the turbulent flows, and pose several difficulties for their experimental [3] or numerical [4] study.

For a wake flow like the one considered, the majority of RANS approaches fails to represent the above-mentioned flow phenomena accurately. Most of the $\kappa - \varepsilon$ models used in the frame of RANS approach tend to overpredict the length of the recirculation region and require several modifications in order to reproduce the experimental observations [1]. For the DNS approach on the other hand, the *Re* number restriction is more severe and for the particular problem it is associated with a considerable cost. For these reasons the flow case was chosen by a group of researchers [5] as a benchmark test case in the frame of LES. None of the researchers though, used the immersed boundary concept to account for the geometry, nor the filtered structure function models [6] or the direct pressure solution presented in the present study.

The main targets of the present work are to (a) verify the potential of the IMB method for time-varying flows (b) verify and expand the predictive capability of the FSF models and advanced wall models for complex flows (c) demonstrate that appropriate choices on code structure, implementation and development techniques can lead to very successful low-cost simulations that can be easily performed even on present-day personal computers.

2. TURBULENCE MODELS

The first simulation attempts were done using the simple Smagorinsky turbulence model [7] which is very well documented and widely applied. When more advanced closure procedures are applied, the usual choice by most of the researchers is the dynamic model [1, 5]. The latter is an extension of the Smagorinsky model which adjusts the value of the Smagorinsky constant locally. The filtered structure function model presented in the present study has been very successfully applied for jets, channels [8] and space developing flows [6] but not for time varying or recirculating flows. It should be noted that in the frame of LES, for the flow under test none of the studies conducted in the past employed the use of the FSF turbulence model presented here.

Therefore, in the present study apart from the Smagorinsky model it was decided to examine also the predictive capability of the FSF model for the flow past a rectangular cylinder. Both models used follow a Boussinesq's type eddy viscosity assumption for the closure of the subgrid scale stresses τ_{ij} according to

$$\tau_{ij} = -2\nu_t \bar{S}_{ij} \tag{1}$$

where $\bar{S}_{ij}$ is the strain rate tensor of the resolved field. For the Smagorinsky model the turbulent viscosity ν_t was computed from

$$\nu_t = (C_s \bar{\Delta} D_z)^2 \sqrt{\bar{S}_{ij}\bar{S}_{ij}} \tag{2}$$

where $\bar{\Delta}$ is a grid related filter width and C_s the Smagorinsky constant. For the present problem, the effect of the constant C_s was investigated in the range $[0.08, 0.12]$. In order to recover the correct asymptotic behaviour close to solid boundaries, damping was introduced through the function D_z. For the cases presented here Van Driest type of damping was used in the form

$$D_z = [1 - e^{-(z^+/A^+)^\alpha}]^\beta \quad \text{and} \quad z^+ = \frac{z u_\tau}{\nu} \tag{3}$$

with $A^+ = 25$. The constants (α, β) of Equation (3) adjust the type of damping and for the present study they were fixed to $(1, 1)$. The estimation of the non-dimensional wall distance z^+ was based on the normal distance and the instantaneous wall shear stress τ_w of the closest elementary boundary surface. The potential of the Smagorinsky model is mainly restricted by the sensitivity on the specification of the constant C_s and the empirical introduction of wall damping.

The filtered structure function model evolved from the structure function model of Metais and Lesieur [9]. Ducros *et al.* [6] proposed the application of a high-pass filter in order to suppress large-scale motion and obtain a better estimation of the energy content at the unresolved scales. In the present study, a Laplacian filter was applied iteratively three times on the velocity field. The subsequent computation of the second-order filtered structure function $\bar{F}_2(\bar{u})$ was performed in three dimensions from the filtered velocity field $\bar{u}^{(3)}$ according to

$$\begin{aligned} \bar{F}_2^{(3)}(\mathbf{x}, \bar{\Delta}, t) = \frac{1}{6} [&\|\bar{u}^{(3)}_{i+1,j,k} - \bar{u}^{(3)}_{i,j,k}\|^2 + \|\bar{u}^{(3)}_{i-1,j,k} - \bar{u}^{(3)}_{i,j,k}\|^2 \\ &+ \|\bar{u}^{(3)}_{i,j+1,k} - \bar{u}^{(3)}_{i,j,k}\|^2 + \|\bar{u}^{(3)}_{i,j,k} - \bar{u}^{(3)}_{i,j-1,k}\|^2 \\ &+ \|\bar{u}^{(3)}_{i,j,k+1} - \bar{u}^{(3)}_{i,j,k}\|^2 + \|\bar{u}^{(3)}_{i,j,k} - \bar{u}^{(3)}_{i,j,k-1}\|^2] \end{aligned} \tag{4}$$

in discretized form. Close to solid boundaries a two-dimensional version of the model was applied depending on the orientation of the boundary surface [8]. In all cases, the computation of the structure function took into account grid non-uniformities [10]. The turbulent viscosity was finally computed according to

$$\nu_\tau^{\mathrm{FSF}}(\mathbf{x}, t) = C_{\mathrm{FSF}} \bar{\Delta} [\bar{F}_2^{(3)}(\mathbf{x}, \bar{\Delta}, t)]^{1/2} \tag{5}$$

where $C_{\mathrm{FSF}} = 0.0014 C_{\mathrm{K}}^{-3/2}$ with $C_{\mathrm{K}} = 0.417$ being the Kolmogorov constant. The great advantage of the FSF model is that although constants are used the model is not sensitive to their specification. Additionally, the FSF model is appropriate for the transitional character of the flow and as it was implemented in the present study it has the correct limiting behaviour close to solid boundaries.

3. NUMERICAL METHOD

One of the main challenges in simulating turbulent flows in geometrically complex domains, is the accurate and fast pressure solution which is usually the most computationally intensive procedure. LES computations are usually performed in very large grids (of the order of

million points) where accurate elliptical solutions are required for thousands of time steps. Therefore, especially in LES apart from geometric flexibility the solvers should also meet the crucial requirements of efficient and parallel execution. The N–S solver developed is capable of meeting these requirements simultaneously.

The rationale behind the design of the code was the use of efficient numerical techniques, so that large-scale computations can be performed using limited computer resources. The numerical method is based on the fractional step technique of Kim and Moin [11]. A staggered variable arrangement is adopted, on structured rectangular grids. The conservation equations for momentum and the derived Poisson's equation for pressure correction are discretized using simple second-order central differences for all terms. Second-order accuracy is preserved at the boundaries of the computational domain, using suitably modified boundary conditions. Explicit time advancement was used for all terms, based on the Adams–Bashforth scheme, using a constant time step Δt.

The core of the numerical code is a fast parallel direct Poisson's solver, which is a modified version of the public domain software package `FISHPAK` [12–14]. The latter was first heavily modified to allow the solution in three-dimensional domains with stretched grids in two directions. Later the solver was optimized and fully parallelized for shared memory architectures. The parallelization strategy was operation oriented. Considering a direct solution on an (Nx,Ny,Nz) computational box, the forward and inverse FFT operations are performed in parallel in $(x–y)$ planes. Similarly, the actual pressure solution on mutually independent two-dimensional Helmholtz planes, is treated naturally in parallel $(x–z)$ planes. The above-mentioned implementation technique eliminates load imbalance and achieves an excellent parallel performance. The full details of the numerical technique can be found in Reference [15].

A special storage procedure was adopted in order to improve data locality and domain identification. The computational variables are stored in one-dimensional arrays exclusively. The cells that correspond to the internal *fluid* part of the domain (denoted as *active*) are stored first. The following memory entries are occupied by fictitious *inactive* cells that compose the domain's boundary surfaces. These cells are sequentially grouped and stored surfacewise. That storage scheme largely simplifies the identification of various parts of the domain eliminating the use of expensive algorithms (including `IF...THEN` statements) to identify boundary surfaces. That finite-element-type numbering minimizes storage requirements since only the active part of the computation is stored in memory. The technique requires the explicit definition of neighbours, through the storage of extra integer arrays. However, the extra computing resources required are negligible compared with the benefits of the topological flexibility and robustness of the algorithm. The physical domain is mapped onto the computational domain in such a way that when solid bodies exist, only the flow domain is kept in memory in contrast with three-dimensional representations where the full rectangular domain has to be stored. Considering the fine grid that is usually employed close to obstacles, the current method can save large amounts of physical memory.

The resulting code requires approximately 150 Mb of physical memory and 2.5 `GFlops`/iter per million computing nodes. Execution performance was 1 μs/node/iter on 8 processors in UNIX environment (V-class HP-9000, HP-UX 11.0), and 3 μs/node/iter on personal computers (PIII-800 MHz, W2000). The efficiency of parallel execution was measured 0.87% on 8 CPUs (speedup of ~ 7). Using Amdahl's law [16] it can be easily shown that parallel implementation reached 97%, which corresponds to a maximum theoretical acceleration of 34. At the moment,

any type of orthogonal geometry can be encountered, while the extension to flows over geometrically arbitrary bodies and moving boundaries is under development.

3.1. Immersed boundary method

The geometric flexibility of the developed solver results from the adoption of the *immersed boundary* concept, and various elements from finite-volume and finite-element formulations. The immersed boundary concept (IMB) method was originally presented in the pioneering work of Peskin [17]. More recently, a simplified version of the method was presented [18, 19]. The basic idea of the method lies on the definition of the solid (either moving or not) boundaries. Instead of using complicated boundary fitted grids to define the geometrical configuration, the immersed boundary method actually *mimics* the presence of solid bodies by means of suitably defined body forces applied to the discretized set of the momentum equations. The N-S set of equations allows the specification of such forcing terms which are introduced through the boundary conditions and inserted as source terms i.e.

$$\frac{D\mathbf{u}}{Dt} = -\nabla P + \nabla \cdot [\nabla \mathbf{u}] + \mathbf{F} \tag{6}$$

The body force $\mathbf{F}$ is computed at every time step, so that the velocity field on an arbitrary surface S is driven to a specified value Γ_S. In general that surface can move and does not necessarily coincide with a grid line. However, in case of a stationary solid body with $\Gamma_S = 0$, the implementation is much simpler, and the discretized form of Equation (6) requires minimum extra effort to account for the presence of one or more bodies [19]. Thus for the cells on the boundary Γ,

$$\mathbf{u}^{n+1} = \mathbf{u}^n + \Delta t(\mathbf{Rhs} + \mathbf{F}) = \Gamma_S \tag{7}$$

where **Rhs** includes all the pressure gradient, advection and diffusion terms. In order to drive the velocity field of the next time step $\mathbf{u}^{n+1}$, to the desired level Γ_S, it is sufficient to formulate the source term $\mathbf{F}$ of the N-S Equation (6) as

$$\mathbf{F} = -\mathbf{Rhs} + \frac{\Gamma_S - \mathbf{u}}{\Delta t} \tag{8}$$

which is imposed appropriately in the discretized form of the conservation equations. In the present study, in order to avoid computational complexities all the grids were constructed so that the grid lines were coincident with the boundary surfaces. Consequently extra uncertainties and inaccuracies that would be introduced by interpolations are eliminated.

In contrast with previous implementations, the conservation equations were not solved inside the solid part at all. The fictitious cells that surround the flow area were used to reproduce the force term $\mathbf{F}$ instead of explicitly specifying forcing in each cell adjacent to a wall boundary. Under these assumptions the implementation of the IMB concept ends up to a consistent definition of boundary conditions. Proper definition of the boundary conditions on the fictitious cells was an adequate condition to ensure the resemblance of a solid boundary and the application of the IMB method. For the present study, second-order boundary conditions were used on all boundaries in order to maintain $O(\Delta x_i^2)$ accuracy at the borders of the computational domain.

In Reference [15] two different methodologies were adopted and examined for the simulation of a turbulent backwards facing step flow. The IMB method was validated and compared with

the domain decomposition approach using the *Schur* complement. Both methods used the same direct pressure solvers and the differences in the predicted properties were less than $\pm 2\%$. Performance monitoring techniques revealed that the IMB method was faster by 30% and required less physical memory. Bearing in mind that it can be easily extended to flows in arbitrary geometry the superiority of the IMB method is evident. The aim of the present paper to demonstrate the potential of that method for time-varying flows.

4. DESCRIPTION OF THE SIMULATIONS

Figure 1 shows the geometrical parameters and the co-ordinate system used for the test case considered. The cylinder is of rectangular cross-section with side dimension d, immersed in a uniform velocity stream u_∞. The resulting characteristic Reynolds number was fixed to 22 000 for all simulations, for direct comparison with the experimental studies of Lyn *et al.* [20] and McLean and Gartshore [21]. According to Reference [5], the dimensions of the computational domain were $(L_i + L_x, L_y, L_z) = (20d, 4d, 14d)$. The rectangular cylinder was located with its axis normal to the oncoming flow at a distance $5d$ from the inlet plane.

4.1. Inflow–outflow-lateral boundary conditions

A uniform stream $u_\infty = 1$ was imposed at the domain's inlet, while both perturbed and unperturbed cases were computed. The outlet plane was located 15 diameters downstream of the body to allow the undisturbed development of the vortex street formation. In order to avoid the distortion of the flow structures leaving the domain and diminish the effect of the exit upstream, the convective boundary condition was used [22] i.e.

$$\frac{\partial u_i}{\partial t} + U_c \frac{\partial u_i}{\partial x} = 0 \tag{9}$$

which is very popular choice in LES computations of space developing flows. The convection velocity U_c was set equal to the free stream velocity u_∞. Equation (9) is usually integrated

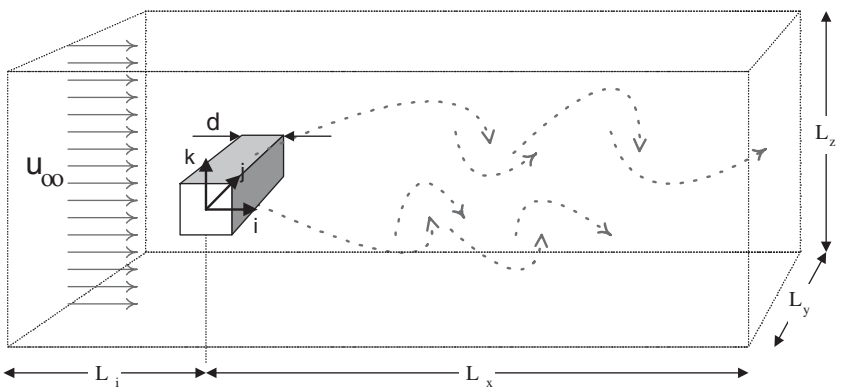

Figure 1. Definition of the co-ordinate system and the geometrical parameters for the plow past a rectangular cylinder.

in time using an explicit approximation. In the present study an implicit Euler scheme was used in time and an upwind approximation in space according to Simons [23].

Periodic boundary conditions were applied for all variables along the spanwise direction (y) along the cylinder's axis. For the direction (z) normal to the flow symmetry conditions were used, i.e. $\mathrm{d}U/\mathrm{d}z = \mathrm{d}V/\mathrm{d}z = 0$ and $W = 0$.

4.2. Solid wall boundary conditions

The numerical resolution used in most cases necessitated the use of an approximate wall boundary condition since the wall region was not adequately resolved. A new approximate wall boundary condition was constructed, which was first validated for simpler separating flows such as the flow over a backwards facing step [15]. The local character of that boundary condition emerges from the perfect correlation that is assumed between the resultant velocity parallel to the wall of the first node closest to the wall $|\vec{u}|_w$ and the instantaneous wall shear stress τ_w at the elementary boundary surface. In that sense the wall boundary condition resembles a 'modified' Werner and Wengle [24] approach.

However, the wall boundary condition presented here promotes the generality and increases the applicability and efficiency of the method. Instead of a typical $\frac{1}{7}$ power law [1] or a zonal approach, Spalding's [25] law of the wall was used which is valid from the sublayer to the intermediate transition layer and up to the logarithmic region. Consequently, throughout the boundary layer from the wall to the free-stream, the same physical law was applied in a general manner. Additionally, the wall model is not based on a predefined velocity direction but adjusts locally according to the local natural direction of the flow.

Although the run time application cost of such methods is usually assumed negligible, performance monitoring techniques in preliminary simulations revealed that due to the computation of exponentials the computing load was as high as 10%. Therefore, it was decided to precompute and store a 'look-up' table containing pair of values for $|\vec{u}|_w \Leftrightarrow \tau_w$. That way of implementation reduced the computational load to less than 0.5% while the overall accuracy of the method was sustained.

4.3. Initial conditions

The initial field for all simulations was a uniform stream $u_\infty = 1$ superimposed with Gaussian random divergence-free perturbations of intensity 2–5% w.r.t. the local value. The set of equations was integrated for 200–250 characteristic times $t_c = d/u_\infty$. After a transient time the flow rejected the initial unrealistic condition and the shear layers at the cylinder's faces initiated vortex shedding. Once the flow indicated an established periodic behaviour, statistics where collected for a period of $100t_c$ and each sample was taken every $0.01t_c$. The period of time corresponds to 10–13 shedding cycles, an adequate time interval to guarantee statistical stationarity [1].

4.4. Computational grids

The grids used for the present study are summarized in Table I. Several numerical resolutions were examined in order to assess the effect of the grid properties on the predicted flow fields. The cylinder's surface was covered from 480 up to 4800 cells. The grid dimensions were similar to the ones presented in References [1, 5]. However, in the present study the

Table I. Parameters of the grids used for the flow around a rectangular cylinder.

Grid	Dimensions $Nx \times Ny \times Nz$	Cylinder's resolution	Maximum resolution $(\Delta x_{\min}, \Delta z_{\min})/d$	Number of cells	Time step Δt
G1	90×12×68	10×10	0.094, 0.100	73440	0.01
G2	120×12×90	14×14	0.070, 0.070	129600	0.005
G3	200×12×120	36×20	0.018, 0.041	288000	0.003
G4	400×16×200	112×38	0.0035, 0.02	1638400	0.001
G5	400×24×172	20×20	0.050, 0.050	1651200	0.002

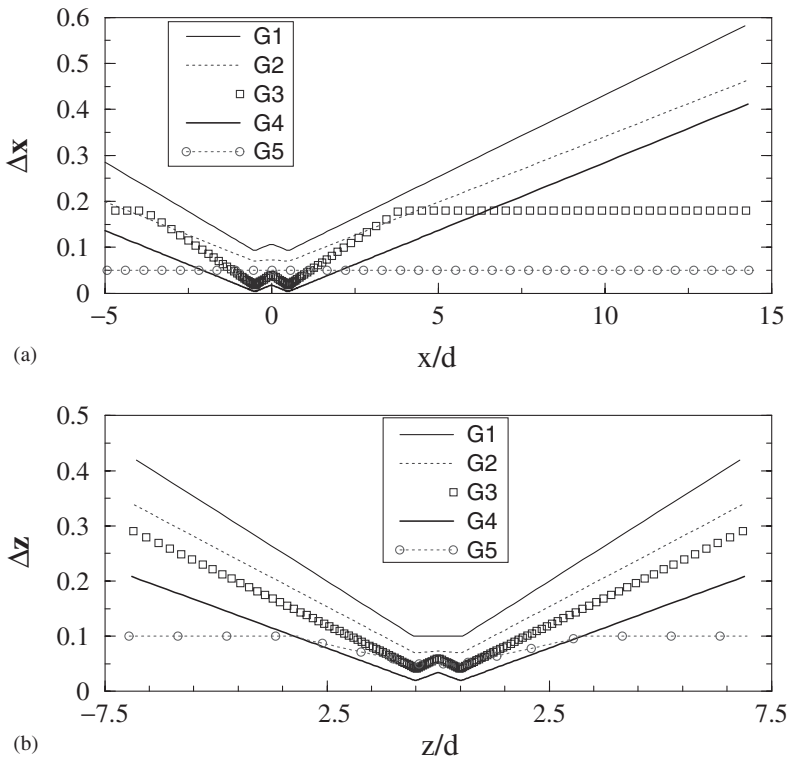

Figure 2. Streamwise and normal grid spacing for the simulations presented (Table I). (a) Grid spacing Δx_i along x direction. (b) Grid spacing Δz_k along z direction.

number of cells resolving the streamwise direction with respect to normal direction is slightly increased. This was done in order to produce isotropic grids with aspect ratios close to unity.

The development of the direct pressure solver (described in Section 3) allowed the use of stretched grids in both the streamwise and normal directions, a feature that proved extremely useful for the fine discretization of the flow close to the cylinder surface. Figure 2 shows the variation of grid spacing Δx_i and Δz_k along (x) and (z) direction. The minimum resolution used in the study was $0.0035d$ while all the grids used were linearly stretched. The expansion

Table II. Table of the examined cases, grids and wall boundary conditions used. Predicted force statistics, average recirculation length, *St* number.

Case, Grid	Wall BC	Model	$\overline{C_L}$	$C_{L_{rms}}$	$\overline{C_D}$	$C_{D_{rms}}$	*St*	X_r
A1, G1	Wall	$C_s = 0.08$	0.011	0.85	2.34	0.153	0.137	1.54
A2, G1	Wall	$C_s = 0.10$	−0.002	0.78	2.22	0.145	0.134	1.81
A3, G1	Wall	$C_s = 0.12$	−0.015	0.55	2.05	0.084	0.128	2.41
A4, G1	Wall	FSF	0.008	0.79	1.96	0.167	0.130	1.68
B1, G2	Wall	$C_s = 0.10$	0.009	0.91	1.99	0.236	0.120	1.44
B2, G2	Wall	FSF	0.013	1.09	2.12	0.286	0.120	1.35
C1, G3	Wall	$C_s = 0.10$	0.037	0.78	2.01	0.190	0.126	1.39
C2, G3	Wall	FSF	0.026	0.84	2.01	0.190	0.126	1.39
D1, G4	No-slip	$C_s = 0.10$	0.009	1.08	1.89	0.085	0.128	1.33
D2, G4	No-slip	FSF	−0.004	1.03	1.95	0.111	0.132	1.35
E1, G5	Wall	$C_s = 0.10$	0.070	1.29	2.10	0.139	0.129	1.28
E2, G5	Wall	FSF	0.011	1.39	2.15	0.165	0.129	1.38
Cheng *et al.*	—	—	—	0.1–0.6	1.9–2.1	0.1–0.2	—	—
McLean *et al.*	—	—	—	0.7–1.4	1.9–2.1	0.1–0.2	—	—
Lyn *et al.*	—	—	—	—	2.1	—	0.132	1.38

coefficient was restricted to 1.03 in order to avoid rapid grid stretching and retain sufficient numerical resolution at the domain's exit.

The advantage of grid stretching in two directions is clearly shown in Table I if one compares cases D and E which employ an equal total number of cells but very different resolution of the cylinder surface. Cases E1 and E2 use a uniform grid with 20×20 cells on the cylinder. On the other hand, the ability to use grid stretching in two directions in cases D1 and D2 increased the cylinder's resolution to 112×38 cells. These cases were the most successful ones overall and due to the high resolution, they used no-slip boundary conditions on the cylinder's walls (Table II). Except cases D1 and D2 all the other cases used the wall boundary condition described in Section 4.2.

4.5. Estimation of global parameters

The major parameters of comparison are the average length of recirculation region X_r and the Strouhal number *St* which is closely related with the accurate reproduction of the vortex shedding mechanism. The latter was as usually computed from the power spectrum of the time history of the lift force coefficient C_L.

In order to evaluate X_r for such a time varying flow, a time-averaged quantity $\Gamma(x,z)$ was defined [15] such that

$$\Gamma(x,z) = \frac{1}{T}\int_0^T \frac{\langle u\rangle_{(x,z)}}{|\langle u\rangle_{(x,z)}|}\,\mathrm{d}t \quad \text{with} \quad \langle u\rangle_{(x,z)} = \int_0^{L_y} u(x,y,z)\,\mathrm{d}y \tag{10}$$

i.e. based on the instantaneous space-averaged velocity along the periodic (y) direction. The integral of Equation (10) can be easily computed in every location (x,z) and is directly related with the probability of the main velocity to be positive ($\Gamma(x,z) = 1$), or negative ($\Gamma(x,z) = -1$). The locus where $\Gamma = 0$ denotes an interface where the velocity was found to be positive as many times as negative (Figure 3). Therefore, the function Γ is directly related

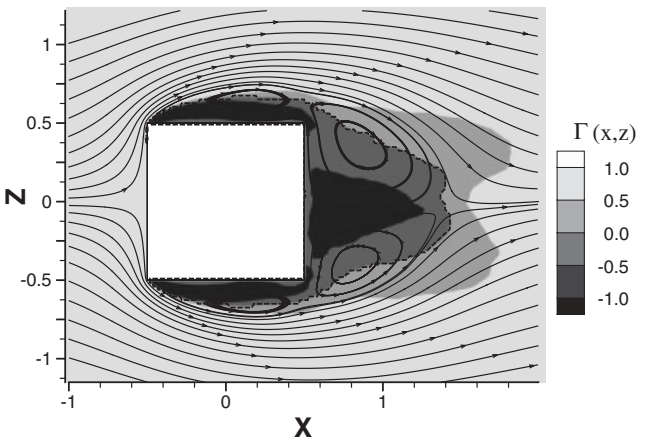

Figure 3. Flow around a rectangular cylinder at $Re_d = 22\,000$. Limits of the recirculation region $\Gamma(x,z)$ and streamlines of the time-averaged mean velocity field. (Grid $400\times16\times200$, FSF turbulence model).

to the location of forward flow fraction used by Le and Moin [26]. The above method of estimating the recirculating region was very successfully used for other cases of wake flows. Apart from generality the method can be easily applied to the whole field and does not require the pre-specification of the area where recirculation is expected. It also gives the opportunity to assess the detailed size and ambiguity of the recirculation area.

5. RESULTS

The cases presented here with their computational parameters are summarized in Table II. Special cases were designed in order to examine the effects of the grid properties and turbulence model. For all the grid resolutions, both models were used in order to compare their predictive capability.

5.1. Global parameters and force coefficients

As shown in Table II the frequency of vortex shedding—as indicated by the *St* number—was found to be in very good agreement with the available experimental data. However, as mentioned by Rodi *et al.* [1] the comparison of *St* numbers is not a safe indication of a successful prediction overall. The results of the present study agree with that statement since that parameter shows a limited sensitivity to the simulation's parameters and for most of the computed cases the predicted *St* number was very close to the experimental value of 0.13. It was observed that the crucial parameter for an accurate prediction of the *St* number was the grid density close to the cylinder and not the overall resolution. This is clearly indicated from cases E1 and E2 where the inadequate wall resolution (20×20 cells) lead to an underestimation similar to the one observed at much lower resolutions (cases B and C).

The time-averaged length of the recirculation region X_r was found to be more sensitive to the simulation parameters. For the lower grid resolutions there was a tendency to overpredict

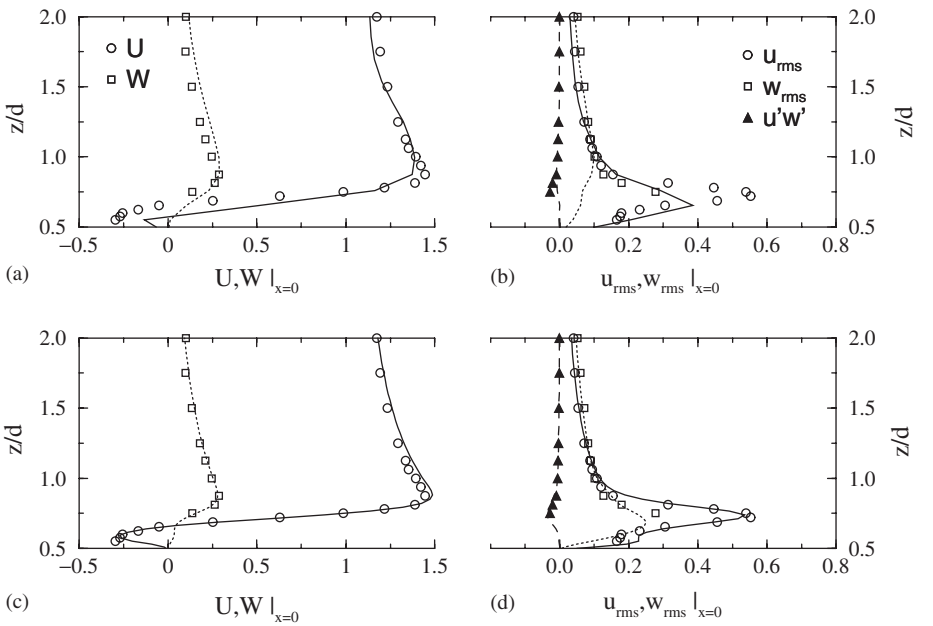

Figure 4. Variation of streamwise, normal velocities and their rms values along the normal axis of the cylinder ($x = 0$). Effect of grid refinement using grids G1 and G4 w.r.t. experimental results. Symbols ($\circ, \square, \triangle$): Lyn and Rodi, lines: FSF model. (a), (b) Time averaged U, W, u_{rms}, w_{rms} with grid G1, case A4. (c), (d) Time averaged U, W, u_{rms}, w_{rms} with grid G4 case D2.

the extend of the recirculation area.[‡] Proper reproduction of the recirculation area was mostly related to the spatial resolution on the cylinder's surfaces especially in the direction of the flow. The shear layers forming on these surfaces and the wake forming after the body play a critical role in the predicted flow regime. Inadequate grid resolution of the shear layers forming at the cylinder's surface, leads to an overestimation of the recirculation length X_{r}. The use of various resolutions indicated that for an acceptable estimation of X_{r}, a minimum grid spacing of at least $0.07d$ should be considered on the surface of the cylinder.

As far as the force statistics of the lift and drag coefficients are concerned, large deviations were noticed. The prediction of their mean and rms values was closely related to the numerical resolution of the shear layers and the use of wall functions. It was evident that insufficient wall resolution or the use of a wall function led to higher values for all the force coefficients. The only exception was the lift coefficient $C_{\mathrm{L_{rms}}}$ which was predicted higher when no-slip conditions were applied in cases D1 and D2. It is interesting to note that in cases A1–A3 the increase of $C_{\mathrm{L_{rms}}}$ was related to a reduced recirculation length X_{r}. In turn X_{r} heavily depends on the separation point along the upper and lower surfaces of the cylinder. As shown in Figure 4(a)–(c) lower resolutions were associated with delayed separation. In these cases the flow remains attached on the cylinder surfaces further downstream. Hence, the pressure and

[‡]It is interesting to note that for other wake flow cases such as backward facing steps, lower resolution leads to an underestimation of the recirculation length.

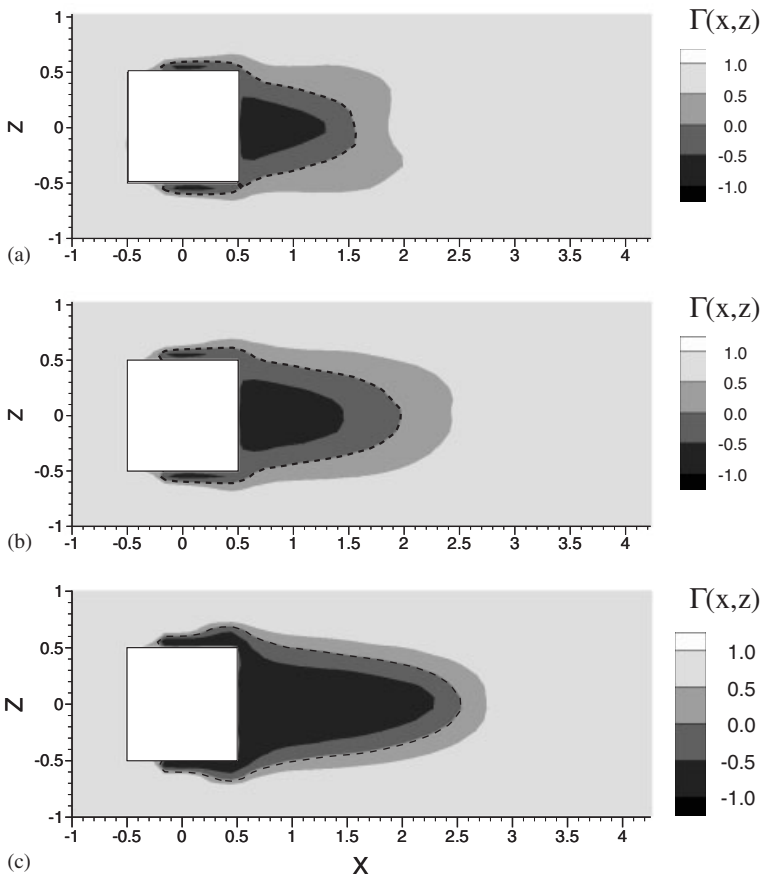

Figure 5. Effect of the Smagorinsky constant C_s on the recirculation region $\Gamma(x,z)$ forming behind the body. Grid G1. (a) recirculation with $C_s = 0.08$ case A1, (b) $C_s = 0.10$ case A2, (c) $C_s = 0.12$ case A3.

lift forces fluctuate on the upper and lower surfaces in a smaller area leading to a reduced value of $C_{L_{rms}}$.

5.2. Turbulence models

Figure 5 shows the effect of altering the value of the Smagorinsky constant from 0.08 to 0.12 for cases A1–A3 (Table II). The size of the recirculation area was found to largely depend on the value of the Smagorinsky constant C_s especially at lower numerical resolutions. A lower constant is associated with reduced energy dissipation of the main flow, which in turns promotes mixing and reduces the wake dimensions and vice versa. However, that tendency recedes for higher resolutions where the model accounts for a narrower range of scales and a smaller part of the total energy transport.

For the same reason the agreement between the two models improved significantly using higher resolutions. Figure 6 shows the comparison of the two models for the time-averaged

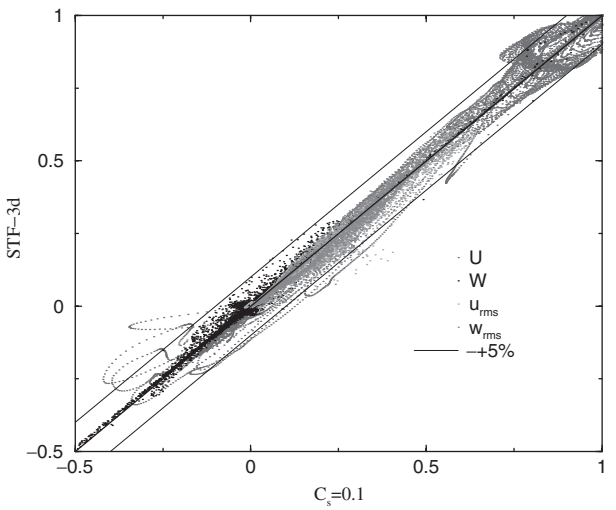

Figure 6. Scatter plot comparing the predictions of the Smagorinsky and FSF turbulence model for the time-averaged flow quantities. A total of 80 000 predicted values for $U, W, u_{\mathrm{rms}}, w_{\mathrm{rms}}$ are plotted for cases E1 and E2 using grid G4.

values using the grid G4. The agreement between the two models was in the range of $\pm 5\%$ for most of the predicted values. The basic difference between the two models concerns the predicted value of X_{r}. For all the computations the FSF model predicted a mean recirculation length closer to the reference value of $1.38d$.

For all the grids examined the FSF model performance was better when compared with the Smagorinsky, in all the parameters of comparison. Additionally, it was always associated with a reduced transient time for the onset of the periodical regime when the computation was starting from scratch. The model was able to adapt faster to a more realistic turbulence field rejecting the initial unrealistic solution. Therefore, its use reduced the total number of iterations required for a complete computation.

5.3. Time-averaged velocity field

The effect of grid refinement on the velocity distribution around the cylinder is illustrated in Figures 4 and 7. For the lower numerical resolutions, the boundary layers forming on the upper and lower walls were less energetic (Figure 4(b)) and tended to separate further downstream (Figure 4(a)). That delay is responsible for the increased recirculation area predicted with coarser grids. For the same reason the location of peak fluctuations in the cylinder's wake is displaced downstream using lower grid resolutions (Figure 7(b)). For the finer grids the location and magnitude of maximum fluctuations are very accurately reproduced showing excellent agreement with the experimental datasets (Figure 7(d)).

The recovery of the mainstream velocity at the core of the wake is shown in Figures 7(a)–(c). Using a finer grid the velocity recovers faster after the cylinder but stabilizes in higher levels when compared to the experiment. In the experimental results the velocity along the

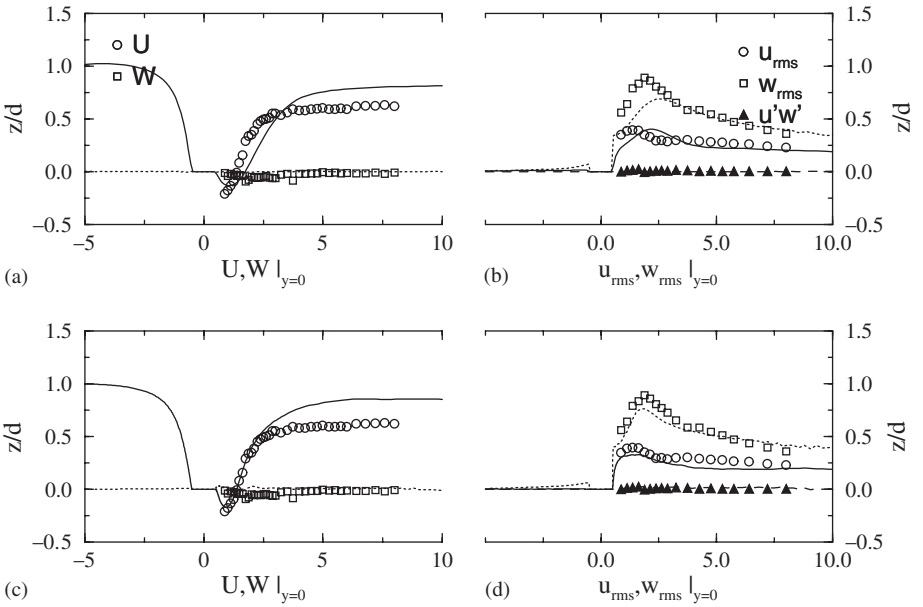

Figure 7. Variation of streamwise, normal velocities and their rms values along the flow direction ($z=0$). Effect of grid refinement using grids G1 and G4 w.r.t. experimental results. Symbols ($\circ, \square, \triangle$): Lyn and Rodi, lines: FSF model. (a), (b) Time averaged U, W, u_{rms}, w_{rms} with grid G1, case A4. (c), (d) Time averaged U, W, u_{rms}, w_{rms} with grid G4 case D2.

centreline levels off at $0.62u_\infty$ at a distance $x>4d$. In the majority of the calculations performed for the present study, the velocity in the same region was predicted higher; around $0.84u_\infty$ irrespectively of the computational parameters. That same difference was also noticed in previous studies conducted for the test case considered [1, 5].

Figures 8 and 9 show the comparison for the mean and fluctuating components of the time-averaged field with the experimental data for cases D1 and D2. The agreement for the streamwise and normal velocity components (Figure 8) is excellent throughout the field. This is also illustrated in Figure 10 that compares contours of streamwise and normal velocities with interpolated experimental data of Lyn *et al.* [20]. The only difference is observed in the core of the flow far away of the cylinder. As mentioned above, the simulations predict a faster core of the flow at the centreline. However, further away from the core of the wake, for distances $|z|>2d$ that difference is eliminated.

As far as the fluctuating components are concerned (Figure 9) the agreement is very satisfactory throughout the field. The width of the wake resembles the one suggested by the experimental data. That agreement is also observed on the upwind face of the cylinder although in the particular case the oncoming flow was unperturbed. The inclusion of a random forcing of intensity 2% at the inlet velocity profiles, did not alter significantly the statistics of the simulated flow. The only effect observed was the faster transition to the time periodic regime, when compared with simulations involving a uniform inlet.

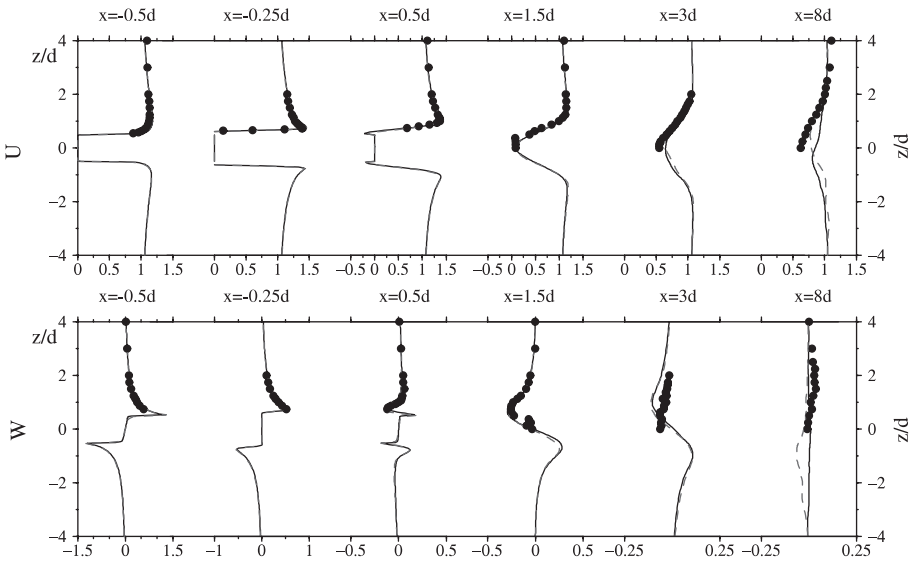

Figure 8. Comparison of the time-averaged streamwise and normal velocity U, W at various locations for the two turbulence models w.r.t. experimental results. (•): Lyn and Rodi (1994),(– – –): Case D1, $C_s = 0.1$, (——): Case D2, FSF.

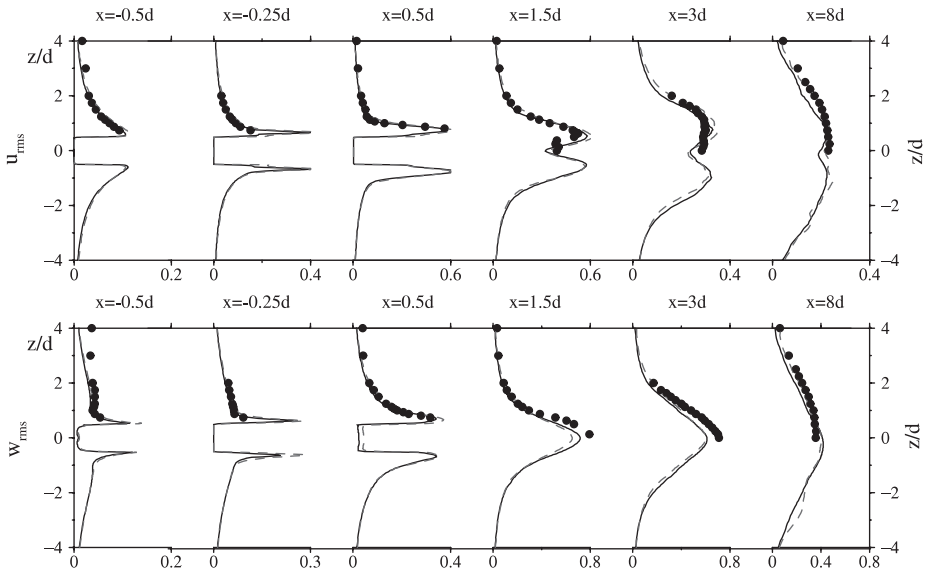

Figure 9. Comparison of the time-averaged streamwise and normal velocity fluctuations u_{rms}, w_{rms} at various locations for the two turbulence models w.r.t. experimental results. (•): Lyn and Rodi (1994), (– – –): Case D1, $C_s = 0.1$, (——): Case D2, FSF.

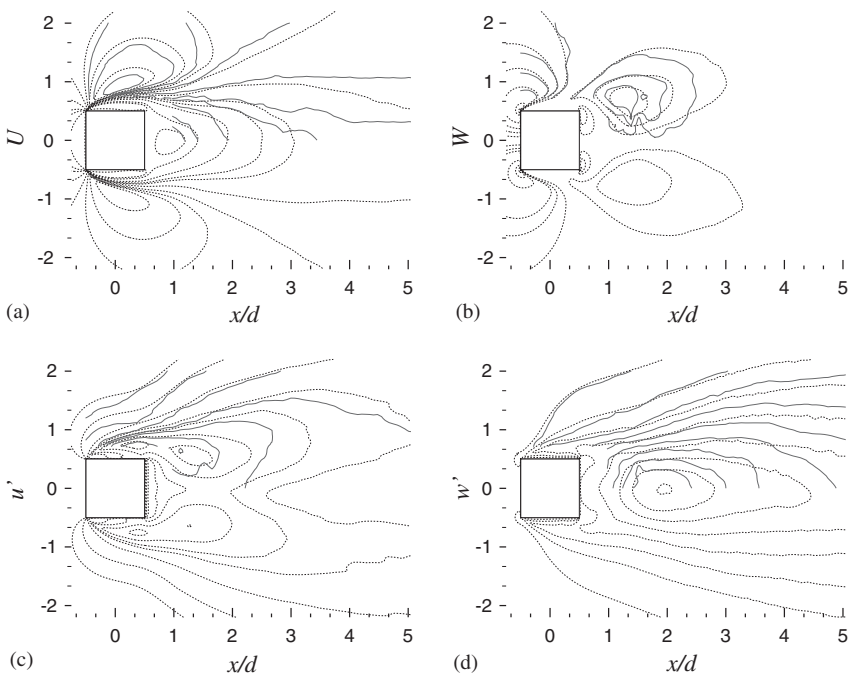

Figure 10. Contours of mean and fluctuating components of streamwise and normal velocities compared with the interpolated experimental data. Solid lines: Lyn *et al.* [20]. Dotted lines: Case D2, no-slip wall boundary condition, FSF turbulence model.

6. CONCLUSIONS

Turbulent flow past a rectangular cylinder has been investigated as a benchmark test case for the development of an efficient parallel code in the frame of large eddy simulations. Apart from the special geometrical treatment applied, the development of a direct parallel pressure solver suitable for complex flows proved to be crucial and beneficial for the efficiency of the numerical code. Combined with the geometrical flexibility offered by the immersed boundary method, low cost computations on grids of the order of several million points were carried out. The underlying philosophy of the numerical design and implementation was 'simpler and much cheaper steps in space and time performed in parallel' which led to affordable large-scale computations.

The overall agreement with the experimental database was very promising for most of the computed cases. Grid sensitivity studies revealed that for the flow case considered the quality of the simulation results largely depends on the resolution of the flow region close to the cylinder's surface. The effect of grid refinement was the strongest of the computational and physical parameters examined. Insufficient grid resolution of the shear layers forming at the cylinder's surfaces, lead to an overestimation of the recirculation area and the drag coefficient C_D.

For global quantities such as recirculation length and Strouhal number the resolution of the cylinder cross-section with 20×20 cells should be considered as minimum. Even in such a low resolution case though, the use of the wall boundary condition described in Section 4.2

led to a very promising agreement with the experimental results. The fluctuating components of the velocity field and the Reynolds stresses required grid spacing smaller than $0.2d$ in the whole filed for satisfactory agreement.

Using higher resolutions several coherent structures were identified during the shedding process. Apart form the main vortices shed from the cylinder, streamwise structures connecting the vortices ('fingers' according to Jordan and Ragab [27]) were also regularly observed [28].

Comparing the predictions of the two turbulence models tested, it appears that the FSF model reached better agreement with the experiments, for all the cases examined. The superiority of the FSF model was mainly due to its ability to account for the transitional character of the flow.

REFERENCES

1. Rodi W, Breuer M, Ferziger JH, Pourquie M. Status of large eddy simulation: results of a workshop. *Journal of Fluids Engineering* 1997; **119**:248–262.
2. Cheng CM, Lu PC, Chen RH. Wind loads on square cylinder in homogeneous turbulent flows. *Journal of Wind Engineering* 1992; **41**:739–749.
3. Okajima A. Strouhal numbers of rectangular cylinders. *Journal of Fluid Mechanics* 1982; **123**:379–398.
4. Davis RW, Moore EF. A numerical study of vortex shedding from rectangles. *Journal of Fluid Mechanics* 1982; **116**:475–506.
5. Voke P. Flow past a square cylinder: test case LES2. In *Direct and Large-Eddy Simulation II*, Chollet JP, Voke PR (eds). Kluwer Academic Publishers: Dordrecht, 1996; 355–373.
6. Ducros FD, Comte PC, Lesieur M. Large-eddy simulation of transition to turbulence in a boundary layer developing spatially over a flat plate. *Journal of Fluid Mechanics* 1996; **326**:1–36.
7. Smagorinsky J. General circulation experiments with the primitive equations, (I) the basic experiment. *Monthly Weather Review* 1963; **91**(3):99–164.
8. Comte PC, Ducros FD, Silvestrini J, David E, Lamballais E, Metais O, Lesieur M. Simulation des Grandes Echelles d'Ecoulements transitionels. *74th AGARD Fluid Dynamics Panel Meeting and Symposium on 'Application of Direct and Large Eddy Simulation to Transition and Turbulence'*, *Chania*, *Crete*, 1994; 14.1-14.12.
9. Metais O, Lesieur M. Spectral large-eddy simulation of isotropic and stably stratified turbulence. *Journal of Fluid Mechanics* 1992; **239**:157–194.
10. Lesieur M, Metais O. New trends in large-eddy simulations of turbulence. *Annual Review of Fluid Mechanics* 1996; **28**(2):45–82.
11. Kim J, Moin P. Application of a fractional-step method to incompressible Navier–Stokes equations. *Journal of Computational Physics* 1985; **59**:308–323.
12. Schumann U. A direct method for the solution of poisson's equation with Neumann boundary conditions on a staggered grid of arbitrary size. *Journal of Computational Physics* 1976; **20**:171–182.
13. Swarztrauber PN. The methods of cyclic reduction, Fourier analysis and the facr algorithm for the discrete solution of poisson's equation on a rectangle. *Journal of Computational Physics* 1977; **19**(3):490–501.
14. Wilhelmson RB, Ericksen JH. Direct solutions for poisson's equation in three dimensions. *Journal of Computational Physics* 1977; **25**:319–331.
15. Grigoriadis D, Goulas A, Bartzis J. Efficient treatment of complex geometries for large eddy simulations of turbulent flows. *Computers and Fluids* 2003; in press.
16. Amdahl GM. Validity of the single processor approach to achieving large scale validity of the single processor approach to achieving large scale computing capabilities. *AFIPS Spring Computer Conference*, Atlantic City, USA, 1967; 483–485.
17. Lai M-C, Peskin CS. An immersed boundary method with formal second order accuracy and reduced numerical viscosity. *Journal of Computational Physics* 2000; **160**:719–750.
18. Mohd-Yusof J. Development of immersed boundary methods for complex geometries. *CTR, Proceedings of the Summer Program*, Stanford University, 1998; 325–335.
19. Verzicco R, Orlandi P, Mohd-Yusof J, Haworth D. Les in complex geometries using boundary body forces. *AIAA Journal* 2000; **38**(3):427–433.
20. Lyn DA, Eivan S, Rodi W, Park JH. A laser-doppler velocimetry study of the ensemble-averaged characteristics of the turbulent wake of a square cylinder. *Journal of Fluid Mechanics* 1995; **304**:285–319.
21. McLean I, Gartshore I. Spanwise correlation of pressure on a rigid square section cylinder. *Journal of Wind Engineering* 1992; **41**:779–808.

22. Pauley LL, Moin P, Reynolds WC. A numerical study of unsteady laminar boundary layer separation. TF-34, Thermoscience Division, Department of Mechanical Engineering, Stanford University, 1988.
23. Simons E. An Efficient multi-domain approach to large eddy simulation of incompressible turbulent flows in complex geometries. *Ph.D.*, Von Karman Institute for Fluid Mechanics, Brussels, 2000.
24. Werner H, Wengle H. Large-eddy simulation of turbulent flow over and around a cube in a flat plate. *Technical Report, 8th Symposium on Turbulent Shear Flows*, September 1991.
25. Spalding D. A single formula for the law of the wall. *Journal of Applied Mechanics*, *Transactions of ASME Series A* 1961; **28**(3):444–458.
26. Le H, Moin P. Direct numerical simulation of turbulent flow over a backward-facing step. *Technical Report TF*-58, Thermoscience Division, Stanford University, California 94305, 1994.
27. Jordan SH, Ragab SA. A large-eddy simulation of the near wake of circular cylinder. *Journal of Fluids Engineering*, *Transactions of ASME* 1998; **120**:243–252.
28. Grigoriadis D, Goulas A, Bartzis J. Efficient large eddy simulations of turbulent flows using the immersed boundary concept. *IUTAM Symposium on Unsteady Separated Flows*, Toulouse, France, April 2002.

